Quantum-like statistics of deterministic wave-particle interactions in a circular cavity

Tristan Gilet[1, *]

[1]*Microfluidics Lab,*
Department of Aerospace and Mechanics,
University of Liège, B-4000 Liège, Belgium

A deterministic low-dimensional iterated map is proposed here to describe the interaction between a bouncing droplet and Faraday waves confined to a circular cavity. Its solutions are investigated theoretically and numerically. The horizontal trajectory of the droplet can be chaotic: it then corresponds to a random walk of average step size equal to half the Faraday wavelength. An analogy is made between the diffusion coefficient of this random walk and the action per unit mass $\hbar/m$ of a quantum particle. The statistics of droplet position and speed are shaped by the cavity eigenmodes, in remarkable agreement with the solution of Schrödinger equation for a quantum particle in a similar potential well.

I.   INTRODUCTION

The interaction between Faraday waves and millimeter-sized bouncing droplets (Fig.1) has attracted much attention over the past decade, owing to its reminiscence of quantum-particle behavior [1, 2]. Faraday waves are stationary capillary waves at the surface of a vertically vibrated liquid bath [3–5]. They appear spontaneously and sustainably when the vibration amplitude exceeds the Faraday threshold. At smaller amplitude, they only appear in response to a finite perturbation (e.g., the impact of a bouncing droplet) and are then exponentially damped [6]. Close to threshold the Faraday instability is often subharmonic, i.e., the Faraday wave frequency is half the frequency of the external vibration [4]. The selected Faraday wavelength λ_F is approximately given by the dispersion relation of water waves. The memory M is defined as the decay time of Faraday waves below threshold, divided by the wave period; it increases and diverges as the threshold is approached.

Liquid droplets are able to bounce several successive times on liquid interfaces before merging, and this in a wide range of conditions [7–9]. Rebounds can be sustained by vertically vibrating the liquid interface [10–14]. When the rebound dynamics locks into a periodic state with one impact every two forcing periods, the droplet becomes a synchronous emitter of Faraday waves [15]. More exactly, the droplet creates a radially propagating circular capillary wave that excites standing Faraday waves in its wake [6]. The resulting wave field then contains contributions from the last M droplet impacts. In the walking state, horizontal momentum is transferred from the wave field to the impacting droplet, proportionally to the local wave slope at the droplet position. The waves only exist in response to droplet impacts, and in turn they cause the horizontal motion of the droplet.
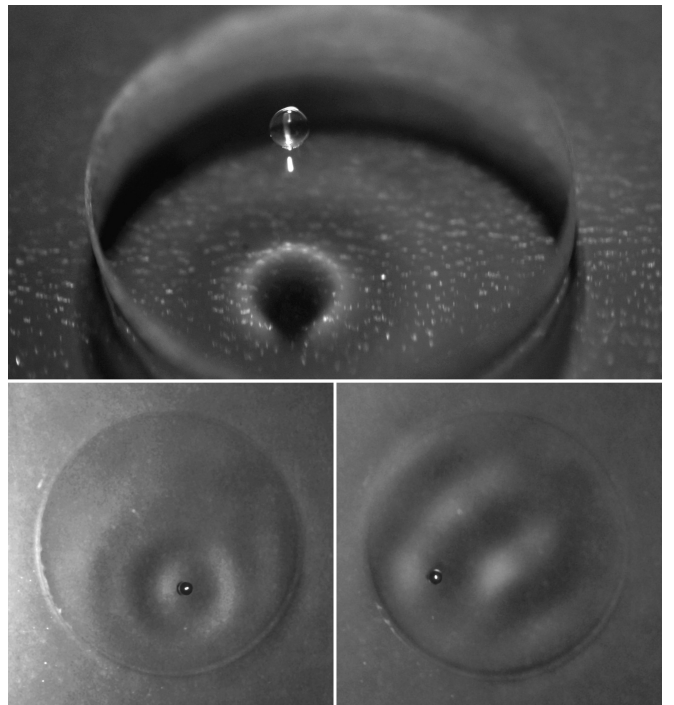

FIG. 1. (top) A drop of silicone oil bounces periodically at the surface of a small pool (diameter 1.5 mm) of the same liquid which is vertically vibrated at 80 Hz. (bottom) Drops of appropriate size (here, diameter of 0.74 mm) can generate and interact with underlying Faraday waves. This wave-particle association is called a walker. The bottom left (right) picture shows a walker at low (resp. high) memory, i.e., far from (close to) the Faraday-instability threshold.

This coupled wave-particle entity at the millimeter scale is called a walker.

The dynamics of individual walkers has been investigated experimentally in several configurations where it has shown properties reminiscent of quantum particles [1]. For example, walkers tunnel through weak boundaries [16]. They diffract or interfere when individually

---

* Tristan.Gilet@ulg.ac.be

passing through one or two slits respectively [17] (although these experimental results have recently been challenged by theoretical arguments [18, 19]). Walkers also experience quantized orbits in response to confinement by either central forces [20], Coriolis forces [21–23] or geometry [24–26]. In the latter case, the walker evolves in a cavity of finite horizontal extent. Chaotic trajectories are often observed in the high-memory limit, when confinement compels the walker to cross its own path again after less than M impacts. In response to central and Coriolis forces, the walker oscillates intermittently between several different quantized orbits, as if it were in a superposition of trajectory eigenstates [22, 27, 28]. The spatial extent of these eigenstates is always close to an integer multiple of half the Faraday wavelength $\lambda_F/2$, which can then be seen as the analog of the de Broglie wavelength for quantum particles [21]. The probability to find the walker in a given state is proportional to the relative amount of time spent in this state. In cavity experiments [24], the probability to find the walker at a given position is strongly shaped by the cavity geometry, as would be the statistical behavior of a quantum particle in a potential well.

Several theoretical models have already been proposed that capture various aspects of walker dynamics [6, 25, 28–31]. Most of them consider a stroboscopic point of view, where the droplet is assumed to impact the bath perfectly periodically. The wave field is then expressed as a sum of contributions from each successive impact [6]. The walker horizontal trajectory is deduced from Newton's second law, where the driving force is proportional to the local wave slope and the effective mass includes both the real droplet mass and an added mass from the wave [32]. The resulting discrete iterated map can be turned into an integrodifferential equation for the walker trajectory in the limit of small horizontal displacements between successive impacts [29]. In an infinite space, the contribution from one droplet impact to the wave field is assumed to be a Bessel function of the first kind $J_0[k_F(\mathbf{x} - \mathbf{x_d})]$ centered on the droplet position $\mathbf{x_d}$, and of wavenumber $k_F = 2\pi/\lambda_F$ [6]. The recent model of Milewski et al. [31] provides a more sophisticated model of the wave fields through inclusion of weak viscous effects. It also includes realistic models of vertical bouncing dynamics [13, 33]. At the other end of the scale of complexity, a generic model [30] has been proposed that reproduces some key features of confined wave-particle coupling and walker dynamics within a minimal mathematical framework. These features include the time decomposition of the chaotic trajectory into eigenstates [28], and the particle statistics being shaped by confinement [24].

These hydrodynamic experiments and models have already revealed a strong analogy between the statistical behavior of chaotic walkers and quantum particles, in many different configurations. It certainly results from the deterministic chaos inherent to such wave-particle coupling. Nevertheless, it is still unclear which ingredients are actually necessary and sufficient for these quantum behaviors to appear. Also, no direct connection between the equations of motion of the walker and the Schrödinger equation has been made yet. What would be the equivalent of Planck's constant for walkers? On which timescale should the walker dynamics be averaged to recover quantum-like statistics? This works aims at answering these questions through a theoretical investigation of walker dynamics under confinement in a two-dimensional cavity [24].

First the model developed in Ref.[30] is particularized to a walker in a circular cavity (Sec. II). In Sec. III the walker dynamics is analyzed as a function of its memory, and results are compared to the experiments of Harris et al. [24]. In Sec. IV it is shown that the present model gives theoretical access to the experimentally-unachievable limit of zero damping (infinite memory) and perfect mode selection. Finally, the above questions are addressed through direct comparison with analytical predictions from quantum mechanics (Sec.V).

II. WAVE-PARTICLE COUPLING IN A CONFINED GEOMETRY

The generic model [30] of the interaction between a particle and a stationary wave confined to a domain S is first recalled, here in a dimensional form. It is primarily based on the decomposition of the standing Faraday wave field $H_n(\mathbf{X})$ resulting from the n first impacts into the discrete basis of eigenmodes $\Phi_k(\mathbf{X})$ of the domain:

$$H_n(\mathbf{X}) = \sum_k W_{k,n}\Phi_k(\mathbf{X}), \quad W_{k,n} = \int_S H_n(\mathbf{X})\Phi_k^*(\mathbf{X})dS,$$

(1)

where Φ_k^* is the conjugate of Φ_k. These eigenmodes are orthonormal on S. They are here chosen to satisfy the Neumann condition $\mathbf{n}\cdot\nabla\Phi_k = 0$ at the boundary ∂S with normal vector $\mathbf{n}$.

We consider the stroboscopic approach where the droplet impacts the liquid bath at regular time intervals. At rebound n, it impacts at position $\mathbf{X}_n$ and creates a crater of shape $Z = F(\mathbf{R})$ in the wave-field. In the limit of a droplet size much smaller than λ_F, the crater $F(\mathbf{R})$ can be approximated by a delta function weighted by the volume of liquid displaced Ω [30]:

$$F(\mathbf{R}) = \Omega \sum_k \Phi_k^*(\mathbf{X}_n)\Phi_k(\mathbf{R}) = \Omega\delta(\mathbf{R} - \mathbf{X}_n).$$

(2)

The contribution $\Omega\Phi_k^*(\mathbf{X}_n)$ of the impact to each wave eigenmode depends on the droplet position.

Each mode $\Phi_k(\mathbf{X})$ is given a viscous damping factor $\mu_k \in [0, 1]$ that depends on the forcing amplitude. It is defined as the amplitude of mode k right before impact $n+1$, divided by its amplitude right after impact n. The associated memory M_k is given by $M_k = -1/\ln\mu_k$. The Faraday threshold instability corresponds to $\max(\mu_k) =$

1. The amplitude of each mode $W_{k,n}$ then satisfies the recurrence relation

$$W_{k,n+1} = \mu_k \left[\Omega \Phi_k^*(\mathbf{X}_n) + W_{k,n} \right] \qquad (3)$$

$$= \Omega \sum_{n'=0}^{n} \mu_k^{n+1-n'} \Phi_k^*(\mathbf{X}_{n'}).$$

At each impact, the particle is shifted proportionally to the gradient of the wave field at the impact position:

$$\mathbf{X}_{n+1} - \mathbf{X}_n = -\delta \sum_k W_{k,n} \left. \nabla \Phi_k \right]_{\mathbf{X}_n} \qquad (4)$$

$$= -\Omega\delta \sum_k \sum_{n'=0}^{n-1} \mu^{n-n'} \left. \Phi_k^* \right]_{\mathbf{X}_{n'}} \left. \nabla \Phi_k \right]_{\mathbf{X}_n},$$

where $\delta > 0$ is the proportionality constant between the local wave slope and the particle displacement. Equations (3) and (4) form an iterated map that describes the evolution of the particle in a cavity of arbitrary shape and dimension.

A. The circular cavity

Focus is now made on a two-dimensional circular cavity of radius R_c, as studied experimentally by Harris et $al.$ [24]. Cavity eigenfunctions are

$$\Phi_{k\ell} = \frac{\phi_{k\ell}}{R_c}, \quad \phi_{k\ell}(r,\theta) = \varphi_{k\ell}(r)e^{ik\theta}, k \in \mathbb{Z}, \ell \in \mathbb{N}_0 \quad (5)$$

where $r = R/R_c$ is the dimensionless radial position, θ is the angular position, and $\phi_{k\ell}$ are the dimensionless eigenfunctions. The dimensionless Faraday wavelength is defined as $\Lambda_F = \lambda_F/R_c$. The radial functions $\varphi_{k\ell}$ are expressed as

$$\varphi_{k\ell}(r) = \frac{1}{\sqrt{\pi \left(1 - \frac{k^2}{z_{k\ell}^2}\right)}} \frac{J_k(z_{k\ell}r)}{J_k(z_{k\ell})}, \qquad (6)$$

where $z_{k\ell}$ is the ℓ-th zero of the derivative of the Bessel function (1st kind) of order k, so $J_k'(z_{k\ell}) = 0$. The integer k can take both negative and positive values. The eigenfunctions satisfy orthonormality conditions

$$\int_0^{2\pi} d\theta \int_0^1 \phi_{k\ell}\phi_{k'\ell'}^* r dr = \delta_{kk'}\delta_{\ell\ell'} \qquad (7)$$

as well as the Neumann boundary condition $\partial_r \phi_{k\ell} = 0$ in $r = 1$. Some of these eigenmodes are illustrated in table I.

The dimensionless Faraday wave field $h_n(r,\theta) = H_n \cdot R_c^2/\Omega$ can be decomposed as a Dini series in this basis:

$$h_n(r,\theta) = \sum_{k=-\infty}^{+\infty} \sum_{\ell=1}^{\infty} w_{k\ell,n}\phi_{k\ell}(r,\theta), \qquad (8)$$

with

$$w_{k\ell,n} = \frac{R_c}{\Omega}W_{k\ell,n} = \int_0^{2\pi} d\theta \int_0^1 h_n(r,\theta)\phi_{k\ell}^* r dr. \qquad (9)$$

The condition $w_{-k\ell,n} = w_{k\ell,n}^*$ results from $h_n(r,\theta)$ being real-valued. Therefore,

$$h_n(r,\theta) = \sum_{k=0}^{+\infty} \sum_{\ell=1}^{\infty} \xi_k \Re \left[w_{k\ell,n}\phi_{k\ell}(r,\theta) \right], \qquad (10)$$

where $\xi_k = 2$ when $k > 0$ and $\xi_k = 1$ when $k = 0$. For the sake of readability, we will remove the factor ξ_k and index ℓ from most notations, keeping in mind that when cylindrical harmonics are involved, functions that depend on k also depend on ℓ. Specifically, the abbreviated sum over k will always refer to a double sum over k and ℓ, from 0 to ∞ and from 1 to ∞ respectively, with inclusion of the factor ξ_k.

The particle position is expressed in cylindrical coordinates $\mathbf{X}_n/R_c = (r_n \cos\theta_n, r_n \sin\theta_n)$. The wave recurrence relation (3) then becomes

$$w_{k,n+1} = \mu_k \left[w_{k,n} + \varphi_k(r_n)e^{-ik\theta_n} \right]. \qquad (11)$$

The trajectory equation (4) can be projected along $\mathbf{X}_n$, then in the direction perpendicular to $\mathbf{X}_n$:

$$r_{n+1}\cos(\theta_{n+1} - \theta_n) = r_n - C \left[\frac{\partial h_n}{\partial r} \right]_{(r_n,\theta_n)}$$

$$r_{n+1}\sin(\theta_{n+1} - \theta_n) = -\frac{C}{r_n} \left[\frac{\partial h_n}{\partial \theta} \right]_{(r_n,\theta_n)}, \qquad (12)$$

where

$$C = \frac{\delta\Omega}{R_c^4} \qquad (13)$$

is a dimensionless constant that characterizes the intensity of the wave-particle coupling. After calculating the gradient of h_n at the impact point, the iterated map becomes

$$r_{n+1}\cos(\theta_{n+1} - \theta_n) = r_n - C \sum_k \varphi_k'(r_n)\Re \left[w_{k,n}e^{ik\theta_n} \right]$$

$$r_{n+1}\sin(\theta_{n+1} - \theta_n) = \frac{C}{r_n} \sum_k k\varphi_k(r_n)\Im \left[w_{k,n}e^{ik\theta_n} \right]$$

$$w_{k,n+1} = \mu_k \left[w_{k,n} + \varphi_k(r_n)e^{-ik\theta_n} \right], \quad (14)$$

where $\varphi'(r) = d\varphi/dr$.

B. Model discussion

This model of walkers neglects traveling capillary waves, similarly to most previous works [6]. Indeed, these waves are not reenergized by the vertical forcing, and their initial energy spreads in two dimensions. Their amplitude is then smaller than Faraday waves, and their

contribution is likely to have only marginal influence on the walker's long-term behavior. Only when the walker comes close to the boundary could these capillary waves significantly modify the local trajectory. But this effect would then be localized in space and time, so we assume that it does not strongly affect the walker statistics.

In contrast to previous models [29, 31], the trajectory equation (4) is here first order in time. It therefore assumes that the walker completely forgets its past velocity at each impact, i.e., horizontal momentum is entirely dissipated. Nevertheless, an inertial effect is still present, because the walker keeps a constant velocity between successive impacts. An additional inertial term, e.g., corresponding to the hydrodynamic boost factor [32], would increase the model complexity and the number of parameters, so it is left to future work.

This model should be compared to the experimental results of a walker in a circular cavity reported by Harris *et al.* [24]. A necessary step to a quantitative comparison is the accurate determination of each eigenmode Φ_k and its associated damping factor μ_k. Unfortunately, these modes are not easily characterized experimentally, since they cannot be excited one at a time. Uncertainty in the boundary conditions further complicates mode identification. Ideal Dirichlet boundary conditions (zero velocity where the liquid-air interface meets the solid walls) could have been expected if the contact line was pinned [34]. But in experiments contact lines are avoided on purpose because the vibration of the associated meniscus would be a source of parasitic capillary waves. Instead, the solid obstacles that provide confinement are always slightly submerged [16, 17, 24, 26]. The walker cannot penetrate these shallow regions since waves are strongly dissipated there [16]. Recent numerical simulations suggest that such boundary condition cannot be strictly expressed as a Robin condition [35]. From a practical point of view, when Dirichlet boundary conditions are considered in Eq.(14), the particle tends to leave the cavity as its radial displacement does not vanish at the boundary. For this reason, Neumann boundary conditions (zero wave slope) are adopted in this work.

Determining the damping factor associated with each mode is also an issue. In the absence of horizontal confinement, viscous wave damping can be estimated by spectral methods [5, 31]. The theoretical prediction is then validated by measuring the Faraday threshold amplitude as a function of forcing frequency. Unfortunately, confinement with submerged vertical walls yields additional viscous dissipation. Indeed, modes $\phi_{k\ell}$ of high k and small ℓ are never observed in experiments right above the Faraday threshold (D. Harris, private communication), while spectral methods would predict them as highly unstable.

TABLE I. Twelve dominant Neumann eigenmodes for a cavity of radius 14.3 mm filled with 20 cS oil and forced at 83 Hz.

Mode	k,ℓ	Λ_F	μ	M	Mode	k,ℓ	Λ_F	μ	M
	2,6	0.31	0.999	738		9,3	0.33	0.983	60
	0,7	0.32	0.998	460		18,1	0.34	0.974	39
	4,5	0.34	0.993	141		10,3	0.32	0.968	32
	13,2	0.33	0.990	99		12,2	0.34	0.962	26
	17,1	0.33	0.989	90		6,4	0.34	0.951	20
	7,4	0.32	0.987	77		5,5	0.32	0.933	15

III. FINITE MEMORY IN A DAMPED WORLD

Harris and co-workers [24] considered a circular cavity of radius $R_c = 14.3$ mm filled with silicone oil of density 965 kg/m³, surface tension $\sigma = 20$ mN/m and kinematic viscosity $\nu = 20$ cS. The forcing frequency $f = 70$ Hz was chosen in relation with the cavity size, such that the most unstable mode at Faraday threshold is one of the radial modes ($k = 0, \ell \neq 0$). In this work, damping factors are approximately determined from a spectral method [5] for this same cavity with Neumann boundary conditions and various forcing frequencies. A frequency of 83Hz is then selected that again gives predominance to one of the purely radial modes. Only modes of damping factor $\mu_k > 0.01$ are retained. The twelve modes of highest damping factor are illustrated in Table I. Their wavelength is always very close to the Faraday wavelength that would result from this forcing frequency in the absence of confinement.

The average walking speed v_w increases with the coupling constant C. In experiments [24], $v_w = 8.66$ mm/s at a forcing frequency of $f = 70$ Hz and at 99% of the Faraday threshold. This corresponds to an average step size $2v_w/f = 0.017R_c$. The same value is obtained when Eq.(14) is solved with $C = 3 \times 10^{-5}$. If we further assume that $\delta \sim 2v_w/f$, the volume of fluid displaced at each impact can be estimated from Eq.(13) to be $\Omega \sim 5$ µL. This volume corresponds to an interface deflection of a few hundred micrometers on a horizontal length scale of a few millimeters. It is one order of magnitude higher than the droplet volume, even when corrected with the boost factor [32].

and rationalized for unconfined walkers [6, 29]. These orbits emerge from the loss of stability of their corresponding fixed point. The radial stability of both fixed points and corresponding orbits is related to $\varrho''(r)$, as already shown in Ref.[30] for the unimodal and unidimensional version of Eqs. (3) and (4). They are usually stable when $\varrho''(r_1) > 0$ (orbits of type A) and unstable when $\varrho''(r_1) < 0$ (orbits of type B). For single frequency forcing, successive orbits of a same type are approximately separated by $\Lambda_F/2$. The convergence of trajectories towards stable orbits of type A involves wobbling, i.e., radial oscillations (Fig. 2).

B. Transition to chaos
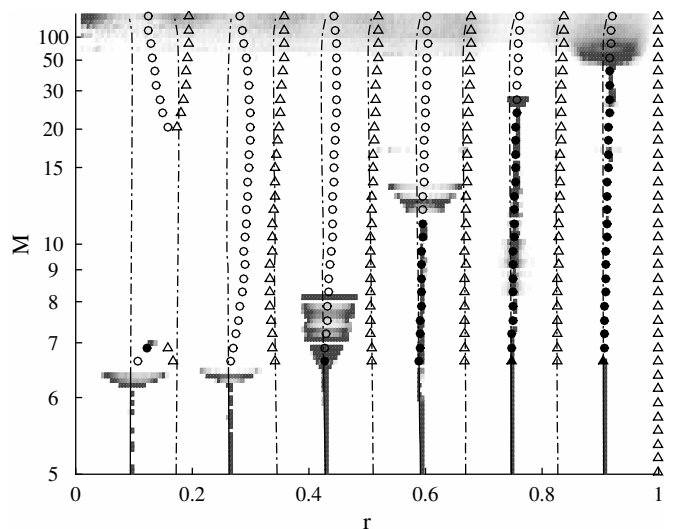
FIG. 3. Bifurcation diagram of the radial position r as a function of memory M at $C = 3 \times 10^{-5}$. The probability distribution function is represented in levels of gray; darker regions correspond to more frequently visited radial positions. Thick solid lines and thin dashed lines correspond to stable and unstable fixed points respectively (Eq. 16). Full and empty symbols represent stable and unstable circular orbits respectively (Eq. 15). Circles ($\circ$) indicate that at least one pair of eigenvalues is complex-conjugated (type A) while triangles ($\triangle$) are used when all corresponding eigenvalues are real-valued (type B).

As memory increases, each circular orbit of type A destabilizes radially through a Neimark-Sacker bifurcation (Fig. 3) [30]. Orbits of larger radius destabilize at higher memory, since it takes more rebounds before the particle revisits its past positions. Sustained wobbling orbits of finite amplitude are then observed, where the radial position oscillates periodically. As memory is increased further, wobbling orbits progressively disappear. At high memory ($M > 50$ in Fig. 3), there are no stable periodic attractors left and the walker chaotically explores the entire cavity. The chaotic nature of
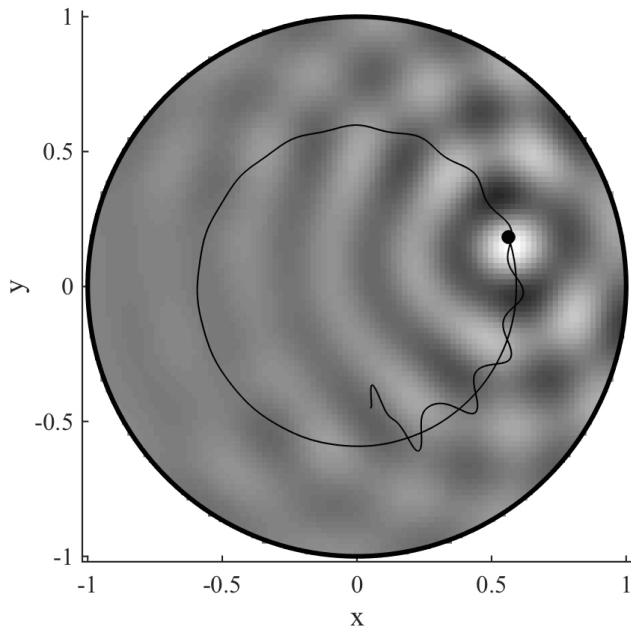

FIG. 2. Convergence to a stable circular orbit of type A ($r_1 = 0.592$, $\alpha = 0.0135$) at memory $M = 7.7$ and $C = 3 \times 10^{-5}$. The underlying wave-field corresponds to the time at which the walker is at the position indicated by the black circle ($\bullet$).

A. Circular orbits

The iterated map (14) admits periodic solutions (Fig. 2) where the particle orbits at constant speed around the center of the cavity: $r_n = r_1$, $\theta_n = \alpha n$ and $w_{k,n} = w_{k1} e^{-ik\alpha n}$ (the wave pattern also rotates). The walking velocity is $r_1 \alpha$. Plugging this solution into the iterated map yields

$$w_{k1} = \frac{\mu_k}{e^{-ik\alpha} - \mu_k} \varphi_{k1} \tag{15}$$

$$r_1(1 - \cos\alpha) = C \sum_k \varphi_{k1} \varphi'_{k1} \mu_k \frac{\cos(k\alpha) - \mu_k}{1 - 2\mu_k \cos(k\alpha) + \mu_k^2}$$

$$r_1^2 \sin\alpha = C \sum_k k \varphi_{k1}^2 \mu_k \frac{\sin(k\alpha)}{1 - 2\mu_k \cos(k\alpha) + \mu_k^2},$$

where $\varphi_{k1} = \varphi_k(r_1)$ and $\varphi'_{k1} = [d\varphi_k/dr]_{(r_1)}$. A detailed analysis of these periodic solutions is given in Appendix A. At low memory, the only solution to Eq.(15) is $\alpha = 0$ (fixed points). The corresponding radii r_1 satisfy

$$\varrho'(r_1) = 0, \text{ with } \varrho(r) = \sum_k \frac{\mu_k}{1 - \mu_k} \frac{\varphi_k^2(r)}{2}. \tag{16}$$

As memory increases (i.e., as all μ_k increase), each of these fixed points experiences a pitchfork bifurcation where two other solutions $\pm\alpha \neq 0$ appear, that correspond to clockwise and counterclockwise orbits. This bifurcation is analogous to the walking threshold observed

the system is highlighted by the exponential growth of the distance between two trajectories that were initially extremely close to one other (positive Lyapunov exponent in Fig. 4).
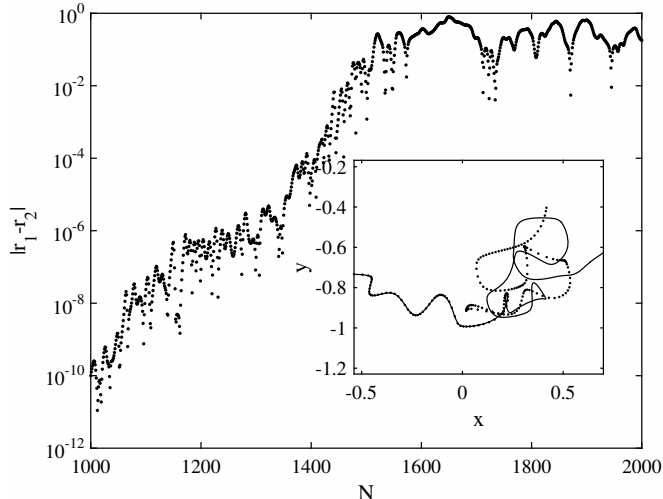

FIG. 4. Exponential divergence of the radial distance $|r_1 - r_2|$ between two neighboring trajectories, initially separated by $|r_1 - r_2| = 10^{-10}$ and placed on the same initial wave-field. Memory and coupling constants are $M = 500$ and $C = 3 \times 10^{-5}$ respectively. (Inset) The two trajectories are represented with a solid line and dots respectively, for $N \in [1400, 1600]$.

A chaotic trajectory is represented in Figure 5. Several trajectory patterns are recurrent, including abrupt changes in direction and off-centered loops of characteristic radius close to half the Faraday wavelength $\Lambda_F/2$. Overall, the walker is observed to spend significantly less time at radial positions where orbits were stable at low memory (Fig. 3).

IV. THE ACCESSIBLE INFINITE MEMORY

Unlike its hydrodynamic analog, a quantum particle confined in a cavity is known to be a Hamiltonian system for which there is no dissipation. The behavior of individual walkers that are reminiscent of quantum particles were always observed at high memory, i.e., when dissipation is almost balanced by external forcing. Indeed, in these conditions, the walker gets a chance to walk onto the wave field left in its own wake [20, 22, 36]. For each mode k, this balance is theoretically achieved when $\mu_k = 1$ (infinite memory). Memory above 100 is very challenging to achieve experimentally, owing to the imperfect control of the forcing vibration [37]. Moreover, in most geometries (including circular) cavities are such that it is impossible to get several modes reaching $\mu_k = 1$ for the same forcing acceleration. This model does not suffer from such limitations; it is possible to select a subset $\mathcal{S}$ of modes for which the memory is in-
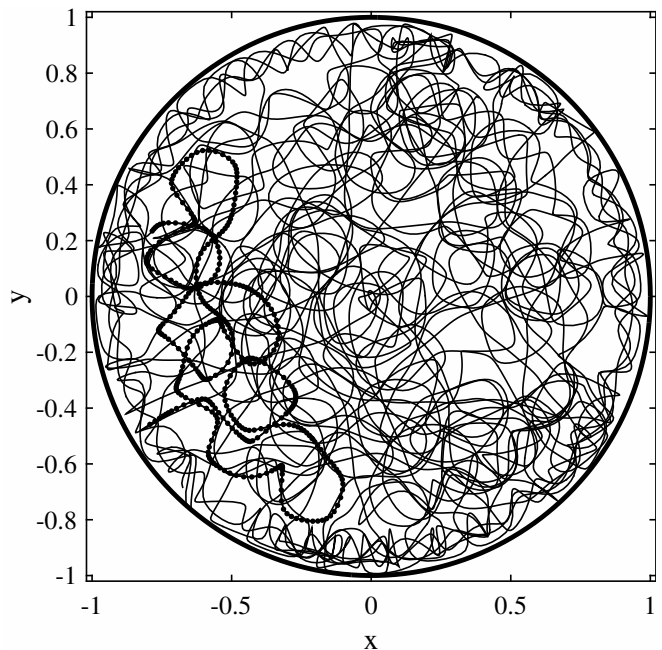

FIG. 5. Chaotic trajectory at memory $M = 500$ and $C = 3 \times 10^{-5}$. The solid line corresponds to 10000 impacts, while the dots emphasize 380 of these successive impacts.

finite ($\mu_k = 1, k \in \mathcal{S}$) while all other modes are instantaneously damped (zero memory, $\mu_k = 0, k \notin \mathcal{S}$). In the following, several subsets of selected modes $\mathcal{S}$ are considered (Table II). Each subset includes all the modes for which the characteristic wavelength lies in a narrow range $\lambda_F \cdot [1 - \Delta\lambda_F, 1 + \Delta\lambda_F]$, except the latest subset which is a combination of two wavelengths. Such mode selection could be analog to preparing quantum particles with localized momentum. For subset $\mathcal{S}_2$ the coupling constant C is varied over four orders of magnitude.

A. Radial statistics

Figure6 shows a superposition of half a million impact positions. Dark circular strips indicate more frequent impacts at certain radial positions r, as observed in experiments [24]. The corresponding probability distribution function $\rho(r)$ shows a series of extrema at radii that are largely independent of C (Fig. 7a). Chaotic trajectories in the infinite memory limit are qualitatively identical to those arising at finite memory. The radial position oscillates intermittently between several preferred radii that correspond to the maxima of $\rho(r)$ [30] (Fig. 7b).

The iterated map is checked to be ergodic to a good approximation (within 1% in these simulations), so the time-average of any property over a single trajectory coincides with an ensemble average of this property over many independent trajectories at a given time. In other

TABLE II. Subsets of selected modes $\mathcal{S}$, corresponding range of wavelength and coupling constant C, and associated symbols and colors in subsequent figures.

	$\mathcal{S}$	Selected modes $(k,\ell) \in \mathcal{S}$	Λ_F	$\Delta\Lambda_F$	$\log_{10} C$
▶	$\mathcal{S}_1$	{(0,5); (2,4); (6,3); (9,2); (13,1)}	0.473	4%	-5
▲	$\mathcal{S}_2$	$\mathcal{S}_1 \cup$ {(3,4); (5,3); (7,3);(10,2);(14,1)}	0.473	8%	-6.5
▲					-6
▲					-5.5
▲					-5
▲					-4.5
▲					-4
▲					-3.5
▲					-3
▲					-2.5
◀	$\mathcal{S}_3$	$\mathcal{S}_2 \cup$ {(1,5); (1,4); (4,4); (4,3); (8,3); (8,2); (11,2); (12,1); (15,1)}	0.473	16%	-5
■	$\mathcal{S}_4$	{(0,12); (2,11); (7,9); (10,8); (13,7); (17,6); (26,3); (30,2); (35,1)}	0.178	1%	-6
•	$\mathcal{S}_5$	{(0,31); (2,30); (11,26); (24,21); (27,20); (47,13); (62,8); (69,6); (77,4)}	0.066	0.2%	-7
⋆	$\mathcal{S}_6$	$\mathcal{S}_1 \cup$ {(0,12); (2,11); (7,9); (13,7); (17,6)}	0.473 + 0.178	4% 0.5%	-5.3

words,

$$\lim_{N\to\infty} \frac{1}{N} \sum_{n'=n}^{n+N} f(r_{n'}, \theta_{n'}) = \int_0^{2\pi} \int_0^1 \rho(r) f(r,\theta) r \, dr \, d\theta.$$
(17)

for any regular function $f(r_n, \theta_n)$. It is rather counterintuitive that the wave-field does not blow up with time, since contributions from previous impacts keep adding up without any of them being damped out. The resulting wave field amplitudes satisfy

$$w_{k,n} = \sum_{n'=0}^{n-1} \varphi_k(r_{n'}) e^{-ik\theta_{n'}}.$$
(18)

In the long term, ergodicity yields

$$\lim_{n\to\infty} w_{k,n} = n \int_0^{2\pi} e^{-ik\theta} d\theta \int_0^1 \rho(r)\varphi_k(r) r \, dr.$$
(19)

The angular integral vanishes by symmetry, except when $k = 0$. In this latter case, the only way to keep a finite wave amplitude is to satisfy

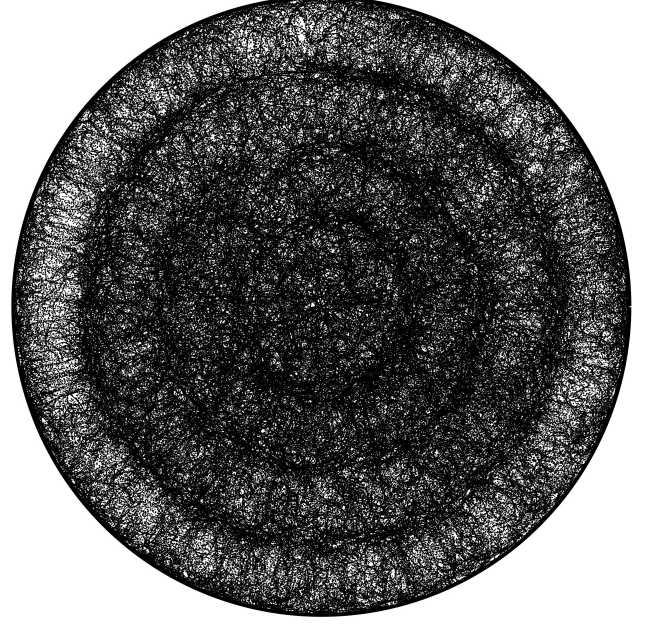$$\int_0^1 \rho(r)\varphi_0(r) r \, dr = 0.$$
(20)

FIG. 6. Two-dimensional probability distribution function obtained by superimposing half a million impact positions issued from 78 independent trajectories. The subset of selected modes is $\mathcal{S}_2$ (Table II), with $C = 10^{-5}$.

So $\rho(r)$ must always be orthogonal to each of the radial eigenmodes $\phi_0(r)$. We have checked numerically that for every subset of selected modes $\mathcal{S}$ (TableII), the component of $\rho(r)$ along $\phi_0(r)$ is always at least two orders of magnitude smaller than the largest other component.

B. Coherence and diffusion

The walker trajectory is usually smooth and regular at the scale of a few impacts (Fig. 5). But such coherence is lost on longer timescales, where the trajectory oscillates and loops chaotically. This behavior is quantified through the average distance $d(n)$ traveled in n steps, defined as

$$d(n) = \sqrt{\langle ||\mathbf{x}_{n'+n} - \mathbf{x}_{n'}||^2 \rangle_{n'}}.$$
(21)

and represented in Figure 8. For small n this distance increases linearly with n so the motion is ballistic (Fig. 8). As soon as $d \gtrsim \Lambda_F/2$, d starts increasing proportionally to $\sqrt{n}$, like in normal diffusion. It then saturates in $d \lesssim 2$ owing to the finite size of the cavity. This ballistic-to-diffusive transition was already observed for the one-dimensional (1D) version of this model [30]. This suggests that the walker trajectory is similar to a random walk for which the elementary steps are of the order of $\Lambda_F/2$.

The average number of impacts in one step should depend on the walker velocity. It can be estimated by first
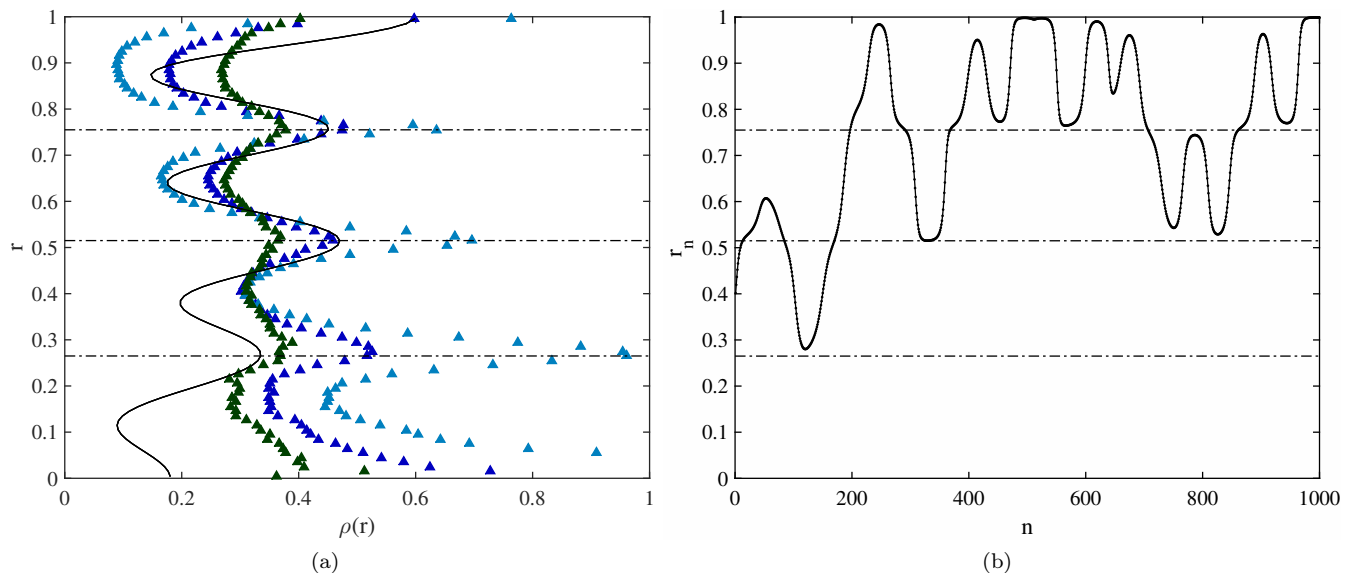
(a)

(b)

FIG. 7. (a) Probability Distribution Function $\rho(r)$ of radial position r, for mode subset $\mathcal{S}_2$ and three different values of C (Table II). The solid line corresponds to the quantum prediction given in Eq.(35). (b) An example of the time evolution of the particle's radial position for mode subset $\mathcal{S}_2$ and for $C = 10^{-5}$.
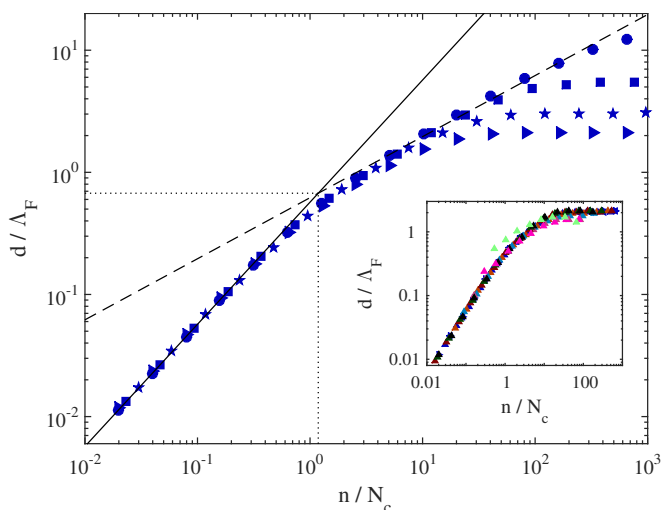

FIG. 8. Average distance d traveled in n successive impacts, for subsets $\mathcal{S}_1$, $\mathcal{S}_4$, $\mathcal{S}_5$ and $\mathcal{S}_6$. The solid line corresponds to the ballistic regime $d/\Lambda_F = an/N_c$, while the dashed line corresponds to the diffusive regime $d/\Lambda_F = b\sqrt{n/N_c}$. (Inset) Same plot, for $\mathcal{S}_1$, $\mathcal{S}_2$ and $\mathcal{S}_3$. Symbols and colors are explained in Table II.

FIG. 9. Average increment of wave amplitude at each impact $\langle|w_{k,n+1}-w_{k,n}|\rangle$ as a function of particle position r, for modes of the subset $\mathcal{S}_2$. The solid line is $|\varphi_k(r)|$. Modes $(k,\ell) = (0,5)$ and $(6,3)$ are represented in black and gray, respectively. Inset shows an example of the time evolution of the wave amplitude $\Re(w_{k,n})$, for these same modes. N_w is defined as the distance between two successive extrema of $w_{k,n}$.

looking at the amplitude $w_{k,n}$ of each wave eigenmode (see inset of Fig. 9). Their time evolution is a succession of coherent linear segments of variable duration N_w. This constant growth rate depends on the particle position; at every impact, each w_k increases by an average amount

$$\langle|w_{k,n+1} - w_{k,n}|\rangle_n \simeq |\varphi_k(r)| \qquad (22)$$
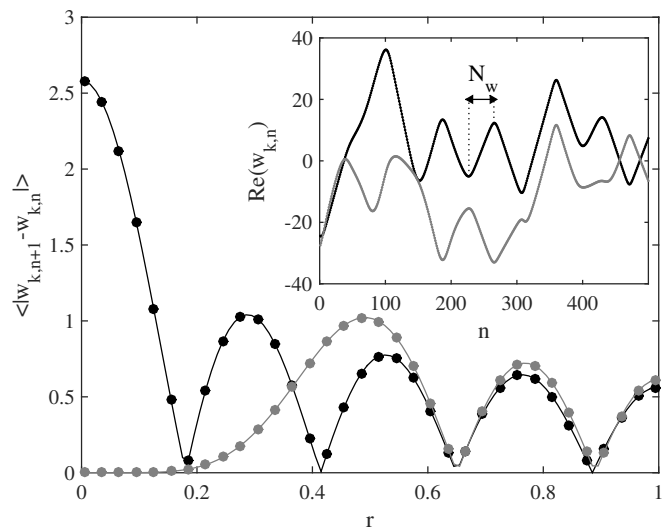
as confirmed in Fig. 9. The statistical distribution of

N_w peaks at approximately the same value for each mode of a given selection, then it decreases exponentially for large N_w (Fig. 10). So after the average coherence time $\langle N_w \rangle$ each mode amplitude w_k has grown by about $\langle N_w \rangle|\varphi_k|$ and its contribution to the total wave slope now scales as $\xi_k w_k \nabla \varphi_k \sim 2\xi_k N_c \varphi_k^2/\Lambda_F$.
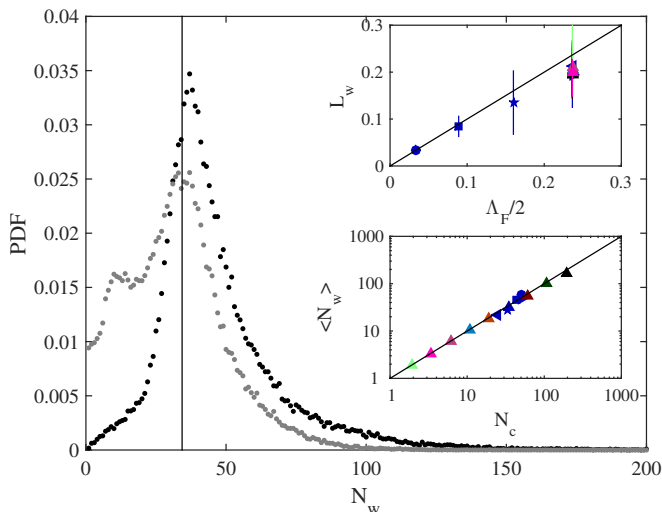
FIG. 10. Probability distribution function of the coherence time N_w, for the two modes $(k, \ell) = (0, 5)$ and $(6, 3)$ of subset $\mathcal{S}_2$ (in black and gray respectively). The vertical line corresponds to $N_w = N_c$ as defined in Eq.(23). Top inset shows average distance L_w traveled during a coherent segment N_w, as a function of the half Faraday wavelength $\Lambda_F/2$. Bottom inset shows average number of impacts $\langle N_w \rangle$ of a coherent segment, as a function of N_c. In both insets, data from all subsets are represented with different symbols (Table II), and the solid line corresponds to equal abscissa and ordinate.

The average displacement per impact is then $\Delta x \sim 2C\chi\langle N_w \rangle \varphi_k^2/(\Lambda_F)$, where $\chi = \sum_k \xi_k$. The average distance $L_w = \sqrt{\langle ||\mathbf{x}_{n'+N_w} - \mathbf{x}_{n'}||^2 \rangle_{n'}}$ traveled during one of these coherent segments is observed to be close to $\Lambda_F/2$, independently of C or $\Delta\Lambda_F$ (see upper inset in Fig. 10). We deduce that $\langle N_w \rangle \sim \Lambda_F/\sqrt{4C\chi\varphi_k^2}$, which yields the definition of the coherence timescale

$$N_c \triangleq \frac{\Lambda_F}{\sqrt{C\chi}} = \frac{\lambda_F R_c}{\sqrt{\delta\Omega\chi}}. \tag{23}$$

The bottom inset of Figure 10 validates the scaling law $\langle N_w \rangle \simeq N_c$ over four decades of C, for several Λ_F and χ, with a proportionality constant almost equal to unity. Even the subset $\mathcal{S}_6$ of mixed wavelengths ($\star$) satisfies these scaling arguments.

The curves of average distance vs time perfectly collapse on a single curve independent of $\Delta\Lambda_F$ (or χ) and C, when n and d are normalized by N_c and Λ_F respectively (see inset of Fig. 8). Only subsets corresponding to $N_c < 4$ (i.e., the two largest values of C for $\mathcal{S}_2$) fail to collapse perfectly. The ballistic regime is described by:

$$\frac{d}{\Lambda_F} = a\frac{n}{N_c} \tag{24}$$

where $a \simeq 0.57$. Similarly the diffusive regime satisfies:

$$\frac{d}{\Lambda_F} = b\sqrt{\frac{n}{N_c}} \tag{25}$$

where $b \simeq 0.62$ based on the data of subset $\mathcal{S}_5$, for which the diffusive region is the largest since Λ_F is the smallest (Fig. 8). If the diffusive behavior is attributed to a two-dimensional (2D) random walk, then the corresponding diffusion coefficient is defined as

$$\tilde{D} \triangleq \frac{d^2}{4n} = \frac{b^2}{4}\frac{\Lambda_F^2}{N_c}. \tag{26}$$

The crossover between both regimes occurs in $n/N_c = b^2/a^2 \simeq 1.2$, so in $d/\Lambda_F = b^2/a \simeq 0.67$. It can be seen as the elementary step of this random walk, and it is slightly larger than half the Faraday wavelength. In dimensional terms, the diffusion coefficient is

$$D = R_c^2 f\tilde{D} = \frac{b^2}{4}\frac{\lambda_F^2 f}{N_c} \simeq 0.096\frac{\lambda_F^2 f}{N_c}, \tag{27}$$

where f is the impact frequency.

V. COMPARISON WITH THE PREDICTIONS OF QUANTUM MECHANICS

In this section, the analogy between walkers at infinite memory and quantum particles is further developed. More exactly, the solutions of the map (14) are compared to the predictions of the Schrödinger equation for a quantum particle subject to the same confinement.

A. Correspondence of timescales

A single quantum particle is statistically described by a wave-function $\Psi(\mathbf{x}, t)$: The probability to find the particle at position $\mathbf{x}$ is given by $\rho(\mathbf{x}, t) = |\Psi|^2$. For nonrelativistic free particles, the wave-function evolves according to the Schrödinger equation

$$i\hbar\partial_t\Psi + \frac{\hbar^2}{2m}\nabla^2\Psi = 0, \tag{28}$$

where $\hbar$ is the reduced Planck constant and m is the rest mass of the particle. Special relativity can be taken into account by instead considering the relativistic Klein-Gordon equation for the function $\psi(\mathbf{x}, t)$, which applies for spinless particles:

$$\frac{1}{c^2}\partial_{tt}\psi + \frac{m^2c^2}{\hbar^2}\psi - \nabla^2\psi = 0. \tag{29}$$

In his pilot-wave theory, de Broglie [38] hypothesized that quantum particles would vibrate at the Compton frequency $\omega_c = mc^2/\hbar$ (Zitterbewegung). The nonrelativistic Schrödinger equation can be retrieved by expressing ψ as the modulation of a nonrelativistic, slowly varying wave function $\Psi(\mathbf{x}, t)$ by this vibration at the Compton frequency:

$$\psi(\mathbf{x}, t) = e^{-i\frac{mc^2}{\hbar}t}\Psi(\mathbf{x}, t). \tag{30}$$

Substitution in Eq.(29) indeed yields

$$i\hbar\partial_t\Psi + \frac{\hbar^2}{2m}\nabla^2\Psi = \frac{\hbar^2}{2mc^2}\partial_{tt}\Psi. \qquad (31)$$

The left hand side is identical to Eq.(28), so the right hand side is a relativistic correction. The characteristic frequency of $\Psi(\mathbf{x},t)$ is $\omega = \hbar k^2/(2m)$. Therefore, the relativistic correction is negligible when $\omega/k \ll c$, or equivalently when $k\lambda_c \ll 1$, where $\lambda_c = 2\pi\hbar/(mc)$ is the Compton wavelength.

Couder and co-workers have already observed in many different configurations [17, 20, 21] that the Faraday wavelength λ_F was the walker equivalent of the de Broglie wavelength $\lambda_{dB} = 2\pi/k$ of quantum particles (Analogy No. 1). In a recent review paper, J.W.M. Bush [1] pushed the analogy one step further and hypothesized that the bouncing motion of walkers could be the equivalent of this Zitterbewegung, so the bouncing frequency f would correspond to the Compton frequency $mc^2/(2\pi\hbar)$ (Analogy No. 2).

The diffusive behavior of the walker on the long term suggests a third analogy (No. 3), between the walker's diffusion coefficient D and the coefficient of Schrödinger equation $\hbar/m$. It is equivalent to say that the Schrödinger timescale $2\pi/\omega = 4\pi m/(\hbar k^2)$ is analogous to the dimensional coherence time of the walker $\lambda_F^2/(\pi D) \simeq [4/(\pi b^2)]N_c f^{-1} \simeq 3.3 N_c f^{-1}$. De Broglie's momentum relation states that the speed of a nonrelativistic particle is $v = \hbar k/m$, which is then equivalent to $[\pi b^2/2]\lambda_F f N_c^{-1} \simeq 0.60\lambda_F f N_c^{-1}$ for the walker. This value is remarkably close to the ballistic speed $a\lambda_F f/N_c$ with $a = 0.57$ as observed in Fig. 8. The analog of the speed of light c is $[b\sqrt{\pi/2}]\lambda_F f N_c^{-1/2} = 0.78\lambda_F f N_c^{-1/2}$, which does not seem to be a fundamental constant in the walker's world. Nevertheless, the relativistic limit $v \to c$ corresponds to $N_c \to \pi b^2/2 \simeq 0.60$ for the walker, i.e., the coherence time becomes of the order of the bouncing period. Saying that a quantum particle cannot go faster than light is then analogous to saying that the coherence time of a walker trajectory should be at least one rebound time. When $N_c = \pi b^2/2 \simeq 0.60$, the equivalent speed of light becomes $\lambda_F f$, which is the phase speed of capillary waves. Finally, in quantum mechanics the correspondence principle states that classical mechanics is recovered in the limit $\hbar \to 0$. This translates into the walker behavior being fully ballistic when D goes to zero, i.e., when the coherence timescale N_c goes to infinity. The three equivalences and their implications are summarized in Table III.

B. Probability density

In a 2D circular infinite potential well of radius R_c, the wave-function can be decomposed into a discrete basis of cylindrical harmonics $\phi_k(\mathbf{r})$ defined in Eq.(5):

$$\Psi = \frac{1}{R_c}\sum_k c_k\phi_k(\mathbf{r})e^{-i\omega_k t}, \qquad (32)$$

where $(R_c^2\nabla^2 + z_k^2)\phi_k = 0$ and

$$\omega_k = \frac{\hbar}{2mR_c^2}z_k^2 \qquad (33)$$

in order to satisfy the Schrödinger equation. The probability density function (PDF) is then

$$\rho(\mathbf{r},t) = \sum_{j,k} c_j^* c_k \phi_j^*(\mathbf{r})\phi_k(\mathbf{r})e^{-i(\omega_k-\omega_j)t}. \qquad (34)$$

Coefficients c_k must satisfy $\int_S \rho dS = \sum_k |c_k|^2 = 1$. Since all z_k are distinct (there is no degeneracy), the time-averaged probability density is

$$\overline{\rho}(\mathbf{r}) = \sum_k |c_k\phi_k(\mathbf{r})|^2 = \sum_k |c_k|^2\varphi_k(r)^2, \qquad (35)$$

which is necessarily axisymmetric. Although all zeros of bessel functions (and derivatives) are strictly distinct, it is always theoretically possible to find and select two eigenmodes (j,k) for which $|z_j - z_k|$ is arbitrarily small. The corresponding imaginary exponential in Eq.(34) would generate some beating at the extremely low frequency $(\omega_j - \omega_k)$ that would challenge any practical computation of a time average. Nevertheless, as far as the modes selected in this work are concerned (Table II), $|z_j - z_k| > 0.01$ for any $j \neq k$.

How well are the walker statistics described by these quantum predictions? Following de Broglie's pilot wave theory [38, 39], we assume an analogy between the quantum wave function and the classical wave field of the walker, averaged over the coherent timescale. In Sec. IV, the walker dynamics was considered in configurations where a small number of modes were equally excited while others were strictly not. This suggests the identification of quantum coefficients c_k as

$$c_k = \frac{\xi_k}{\sqrt{\sum_k \xi_k^2}} \qquad (36)$$

where again $\xi_k = 1$ if $k = 0$ and $\xi_k = 2$ otherwise. As seen in Fig. 7a, the corresponding quantum prediction of the average probability density (Eq. 35) is reminiscent but not identical to the one obtained from walker simulations. Nevertheless, their extrema of density coincide almost perfectly.

C. Average kinetic energy

In quantum mechanics, the kinetic energy operator $\hat{T} = -\frac{\hbar^2}{2m}\nabla^2$ is Hermitian, and its expected value

$$\langle T \rangle = \langle \Psi|\hat{T}|\Psi \rangle = -\frac{\hbar^2}{2m}\int_S \Psi^*\nabla^2\Psi dS = \frac{\hbar^2}{2mR_c^2}\sum_k |c_k|^2 z_k^2 \qquad (37)$$

TABLE III. Correspondence of variables between walkers and quantum particles ($b \simeq 0.62$).

Analogy	Walker			Quantum particle	
# 1	Faraday wavelength		λ_F	de Broglie wavelength	$2\pi/k$
# 2	Bouncing frequency		f	Zitterbewegung frequency	$mc^2/(2\pi\hbar)$
# 3	Diffusion coefficient		$D = [b^2/4]\lambda_F^2 f N_c^{-1}$	Schrödinger diffusion	$\hbar/m$
Derived	Coherence time	$[4/(\pi b^2)]N_c f^{-1}$		Schrödinger timescale	$4\pi m/(\hbar k^2)$
	Ballistic speed	$v = [\pi b^2/2]\lambda_F f N_c^{-1}$		Quantum speed	$v = \hbar k/m$
	Maximum speed	$[b\sqrt{\pi/2}]\lambda_F f N_c^{-1/2}$		Speed of light	c
	Relativistic limit	$N_c > \pi b^2/2$		Relativistic limit	$v/c < 1$
	Ballistic limit	$N_c \to \infty$		Classical limit	$\hbar \to 0$

is time-independent in a infinite potential well. A dimensionless kinetic energy can then be defined based on the cavity radius R_c and Compton frequency $\omega_c/(2\pi)$:

$$\widetilde{T} = \frac{2}{m}\langle T\rangle \frac{4\pi^2}{R_c^2\omega_c^2} = B^2\sum_k |c_k|^2 z_k^2 \tag{38}$$

where $B = 2\pi\hbar/(mR_c^2\omega_c)$ is a dimensionless coefficient. According to Table III, B is equivalent to the dimensionless diffusion coefficient $\tilde{D}$ of the walker, defined in Eqs. (26) and (27). This quantum prediction is in remarkable agreement with the observed average kinetic energy of simulated walkers, for all considered mode subsets (Fig. 11). Only simulations at large C fail to match the prediction, possibly because they would be in the relativistic regime ($N_c < 5$). The energy of the mixed-mode subset $\mathcal{S}_6$ is also overestimated. The kinetic energy of two interacting walkers was shown to be somehow equivalent to the energy stored in the corresponding wave field [40]. Nevertheless, as detailed in Appendix B, it is here unclear if both energies are still equivalent for a single walker confined in a cavity.

FIG. 11. Average dimensionless kinetic energy $\widetilde{T}$ of the walker, vs quantum prediction, with the equivalence $B \equiv \tilde{D}$. Symbols correspond to different mode subsets (Table II). The solid line is the quantum prediction (Eq. 38).

D. Position-dependent statistics

Radial- and azimuthal-velocity operators are defined by projecting the momentum operator $\hat{\mathbf{P}} = -i\hbar\nabla$ along the radial and azimuthal directions, respectively:

$$\hat{V}_r = \tfrac{1}{m}\mathbf{e_r}\cdot\hat{\mathbf{P}} = -i\frac{\hbar}{mR_c}\partial_r,$$
$$\hat{V}_\theta = \tfrac{1}{m}\mathbf{e}_\theta\cdot\hat{\mathbf{P}} = -i\frac{\hbar}{mR_c}\frac{1}{r}\partial_\theta \tag{39}$$

On the one hand, the radial-velocity operator is not Hermitian, so it should not be observable. On the other hand, the tangential-velocity operator has a trivial expected value of zero, by symmetry. The Heisenberg uncertainty principle states that one cannot measure accurately and simultaneously both the position and momentum of a quantum particle. However, it is possible to
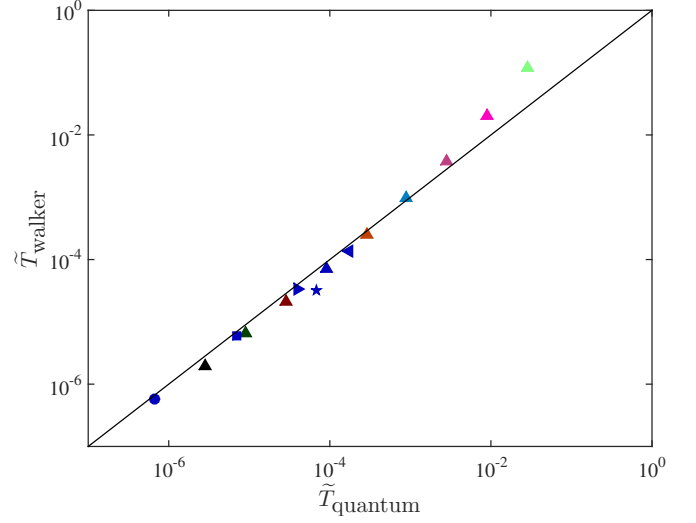
"weakly" measure a quantum particle, gaining some information about its momentum without appreciably disturbing it, so its position can be "strongly" measured directly after [41]. The information obtained from individual measurements is limited. But one can perform many trials, then postselect particles that were observed at a given position and calculate their associated average momentum. We here propose to extend this concept of weak measurement to a particle in a 2D circular cavity. We define the Hermitian operators

$$\hat{V}_r^2 = \hat{V}_r^\dagger \frac{\hat{\delta}(r-R)}{2\pi R}\hat{V}_r \quad \text{and} \quad \hat{V}_\theta^2 = \hat{V}_\theta^\dagger \frac{\hat{\delta}(r-R)}{2\pi R}\hat{V}_\theta. \tag{40}$$

which are aimed to represent the squared radial and azimuthal velocities at a given radial position R, respec-

tively. Their expected values

$$\langle\Psi|\hat{V}_r^2|\Psi\rangle = \left(\frac{\hbar}{mR_c}\right)^2 \int_S \partial_r\Psi^*\partial_r\Psi\frac{\delta(r-R)}{2\pi R}dS, \quad (41)$$

$$\langle\Psi|\hat{V}_\theta^2|\Psi\rangle = \left(\frac{\hbar}{mR_c}\right)^2 \int_S \partial_\theta\Psi^*\partial_\theta\Psi\frac{\delta(r-R)}{2\pi R}r^{-2}dS$$

correspond to the variance of each velocity component. They are time-averaged

$$\overline{\langle\Psi|\hat{V}_r^2|\Psi\rangle} = \left(\frac{\hbar}{mR_c}\right)^2 \sum_k |c_k|^2 [\partial_r\varphi_k]_{r=R}^2, \quad (42)$$

$$\overline{\langle\Psi|\hat{V}_\theta^2|\Psi\rangle} = \left(\frac{\hbar}{mR_c}\right)^2 \sum_k |c_k|^2 k^2 [\varphi_k]_{r=R}^2, \quad (43)$$

and made dimensionless

$$\widetilde{v_r^2} = \overline{\langle\Psi|\hat{V}_r^2|\Psi\rangle}\frac{4\pi^2}{R_c^2\omega_c^2} = B^2\sum_k |c_k|^2 [\partial_r\varphi_k]_{r=R}^2,$$

$$\widetilde{v_\theta^2} = \overline{\langle\Psi|\hat{V}_\theta^2|\Psi\rangle}\frac{4\pi^2}{R_c^2\omega_c^2} = B^2\sum_k |c_k|^2 k^2 [\varphi_k]_{r=R}^2. \quad (44)$$

FIG. 13. Average variance of the tangential velocity $\widetilde{v_\theta^2}$ of the walker at a given radial position r, normalized by $\tilde{D}^2$, for subset $\mathcal{S}_2$ (Table II). The solid line corresponds to 2.0 times the quantum prediction [Eq. (44); best fit].
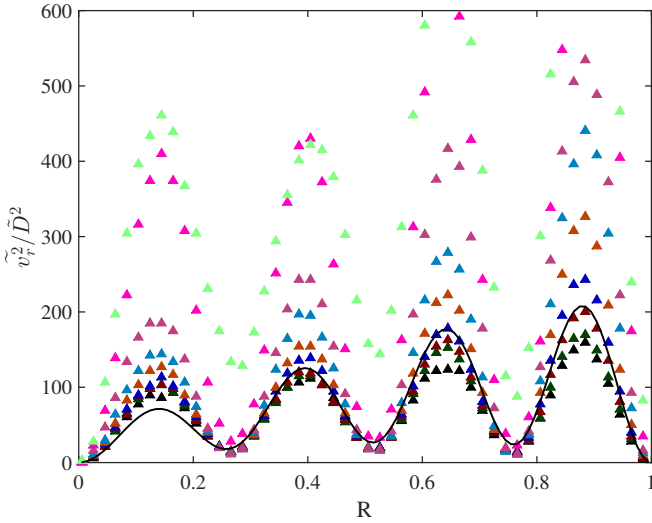

FIG. 12. Average variance of the radial velocity $\widetilde{v_r^2}$ of the walker at a given radial position r, normalized by $\tilde{D}^2$, for subset $\mathcal{S}_2$ (Table II). The solid line corresponds to 3.16 times the quantum prediction [Eq. (44); best fit].

Again, the equivalence between B and $\tilde{D}$ allows for a direct comparison between walkers and quantum predictions. The evolution of $\widetilde{v_r^2}$ with R is very similar in both worlds, although the proportionality coefficient between both (best fit) varies from one subset to another (Fig. 12). The agreement is even better for $\widetilde{v_\theta^2}$, where the walker variance is almost exactly twice the quantum prediction, at any radial position for most values of C (Fig. 13). This remarkable similarity holds for any of the markedly different functions $\widetilde{v_\theta^2}(R)$ at each mode subset
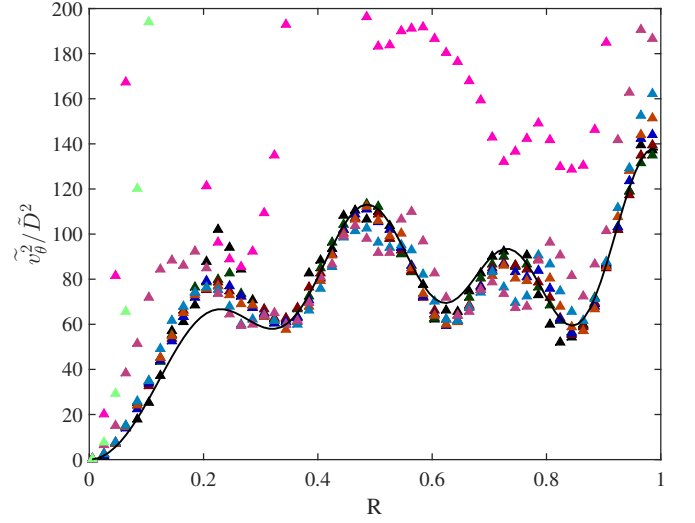
considered (Fig. 14). However, the quantum calculation strongly underestimates both walker variances at large C (relativistic regime).

These results demonstrate how much the velocity statistics of the walker are shaped by the wave function in almost the same way as the statistics of a quantum particle would be. Moreover, they lead to an interpretation of the Heisenberg uncertainty principle for walkers (slightly different from the one proposed in Ref.[17]). The uncertainty in position can be related to the coherence length and it is then of the order of $\lambda_F/2$ (equivalently $\lambda_{dB}/2$). The uncertainty in speed is directly given by the dimensional version of the standard deviation $\sqrt{\widetilde{v}}$, which scales as D/λ_F [equivalently $\hbar/(m\lambda_{dB})$]. The product of these uncertainties then scales as the diffusion coefficient D, which is equivalent to $\hbar/m$. So the uncertainty principle is recovered for walkers provided their dynamics is analyzed at the scale of diffusion.

VI. DISCUSSION

The theoretical framework introduced in Sec.II is one of the simplest mathematical representations of a particle coupled to a wave. It qualitatively captures the key features observed in the experiments on confined walkers performed by Harris *et al.* [24]. It reproduces both the circular orbits at low memory and the chaotic trajectories at high memory. The current limitation for a quantitative comparison originates in the lack of experimental information about the damping rate of each eigenmode. Nevertheless, this model allows for the exploration of regimes that are not accessible experimentally.
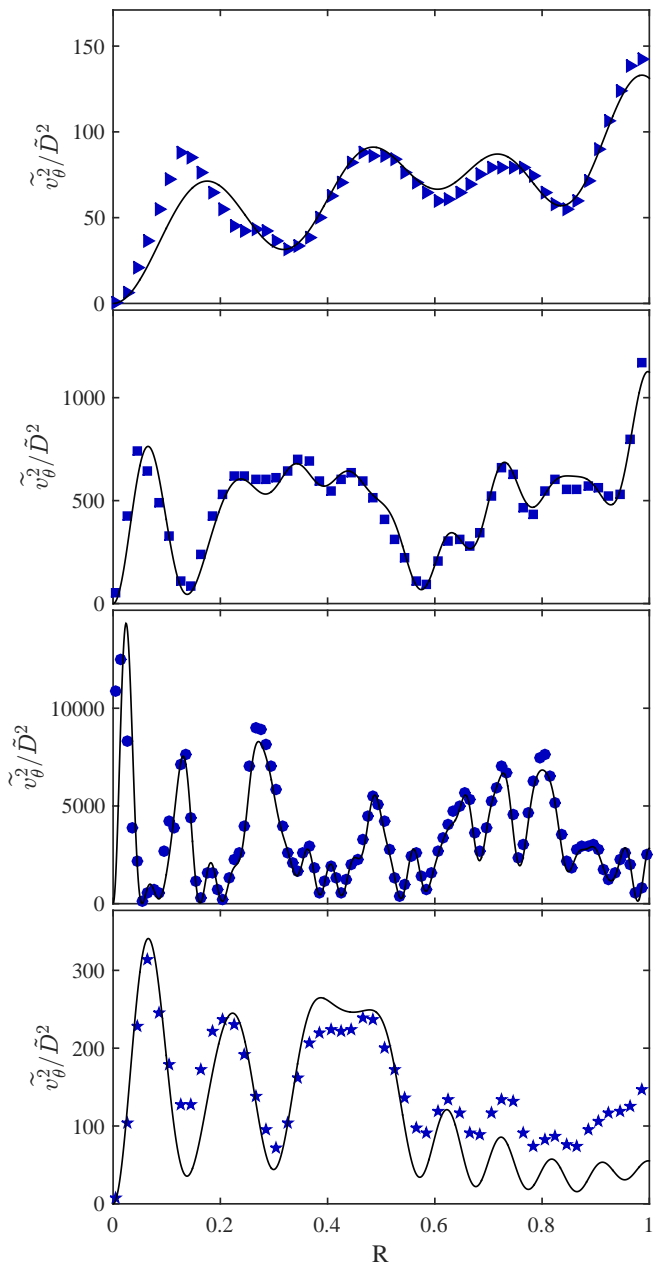
as analogous to the preparation of a quantum state with a more-or-less defined momentum. Nevertheless, it must be noted that this walker model is still highly dissipative since the nonselected modes (the ones that do not resonate with the forcing) are immediately damped.

The chaotic trajectories of confined walkers are ballistic on the short term and diffusive on the long term. The coherence distance, beyond which the ballistic behavior is lost, corresponds to half the Faraday wavelength, as a careful qualitative look at the experimental data [24] also confirms. The Faraday wavelength is at the heart of most quantum-like behaviors of walkers; it is identified as equivalent to the de Broglie wavelength for a quantum particle. Our analysis of the diffusive motion in a circular corral has suggested another equivalence, between the diffusion coefficient D and the factor $\hbar/m$ in the Schrödinger equation. The walker behavior thus becomes apparently random only when it is analyzed at a length scale larger than $\lambda_F/2$. This analogy is confirmed by the observed ballistic speed of the walker, which corresponds closely to the de Broglie speed $\hbar k/m$. Similarly, the average kinetic energy of the walker matches Schrödinger's prediction over several orders of magnitude.

The bouncing dynamics of the walkers was previously hypothesized as reminiscent of the Zitterbewegung of quantum particles [1]. From there, we found an analog for the speed of light in the walker's world, and we then identified the condition for observing relativistic effects on walkers: they have to travel a distance comparable to half the Faraday wavelength at every rebound. Our mathematical framework allows for a future investigation of this regime, which is unfortunately not attainable in experiments where the walking steps are usually limited to around $\lambda_F/20$ [6, 24]. Equivalence relations of TableIII do not explicitly depend on the dispersion relation of the waves. Nevertheless, the variables therein (such as the coherence time or the elementary diffusion coefficient) do depend on the considered wave-particle interaction, e.g., here through the coupling constant C [Eq. (23)]. This might be the reason why the analogs for the speed of light and the Planck constant are not constant in the walker's world.

Harris *et al.* [24] observed that the statistics of confined walkers can be shaped by the cavity eigenmodes in the high-memory limit. We have here calculated the position-dependent variance of walker velocity in the limit of some modes having an infinite memory. Their dependence on radial position is remarkably close to the predictions obtained from the quantum formalism (linear Schrödinger equation) with Hermitian observables, even when complex combinations of modes are considered.

This model of walkers is reminiscent of the pilot-wave theories of de Broglie and Bohm, although there are some significant differences [1]. In the Bohmian mechanical description of quantum mechanics, particles are guided by a pilot-wave prescribed by Schrödinger's equation. It thus evolves at the Schrödinger timescale. The particles do not exert any direct individual feedback on this wave;

FIG. 14. Variance of the tangential velocity $\widetilde{v_\theta^2}$ of the walker at a given radial position r, normalized by $\tilde{D}^2$, for subsets $\mathcal{S}_1$, $\mathcal{S}_4$, $\mathcal{S}_5$, and $\mathcal{S}_6$, from top to bottom (Table II). The solid lines in correspond, respectively, to 1.0, 2.1, 2.2 and 2.0 times the quantum prediction associated with each subset [Eq. (44); best fit].

Of particular interest is the possibility to set the memory of each mode to either infinity (no damping) or zero (full damping). Quantumlike behavior of individual walkers were observed at high-memory, when the system was as close to conservative as it can be. In this model, the mode selection around one given wavelength can be seen

only their statistics shapes the wave. By contrast, individual bouncing walkers locally excite the wave field that sets them into motion. The double-solution theory of de Broglie [38] involves an additional pilot-wave centered on the particle, whose timescale would be the Zitterbewegung period. This second wave could be the analog of the real Faraday wave that couples with individual walkers. It was already shown that the Schrödinger equation can be retrieved from a random walk of diffusion coefficient $\hbar/(2m)$ [42]. This work suggests that such a random walk can originate from the chaos of a deterministic map that describes the coupling of a wave and a particle. In other words, the solution of Schrödinger equation for a particle in a cavity can be obtained from a purely deterministic mechanism that does not involve any stochastic element.

Walkers have now been investigated for a decade. They have shown many behaviors reminiscent of quantum particles. We have shown here that, when they are confined in cavities, their statistics closely approaches the solution of the Schrödinger equation. Future work is still required to identify the exact limits of this analogy.

Appendix A: Stability of fixed points and orbits

1. Finite memory

Fixed points of the iterated map (14) satisfy $r_n = r_0$ and $w_{k,n} = w_{k0}$. Because of axisymmetry, θ_n can take any constant value, so the locus of these fixed points is a series of concentric circles, referred to here as fixed lines. The iterated map then becomes

$$w_{k0} = \frac{\mu_k}{1-\mu_k}\varphi_{k0} \quad \in \mathbb{R}$$
$$\sum_k \frac{\mu_k}{1-\mu_k}\varphi_{k0}\varphi'_{k0} = 0 \qquad (A1)$$

where $\varphi_{k0} = \varphi_k(r_0)$ and $\varphi'_{k0} = [d\varphi_k/dr]_{r_0}$. This second condition can be written $\varrho'(r_0) = 0$ with

$$\varrho(r) = \sum_k \frac{\mu_k}{1-\mu_k}\frac{\varphi_k^2(r)}{2} \qquad (A2)$$

Stability of these solutions can be inferred from a linearized version of the map for small perturbations: $r_n = r_0 + \tilde{r}_n$, $\theta_n = \tilde{\theta}_n$, $w_{kn} = w_{k0} + \tilde{w}_{kn}$, where $\tilde{x}_n \ll 1$, $\tilde{\theta}_n \ll 1$ and $\tilde{w}_{kn} \ll 1$. We also decompose $\tilde{w}_{kn} = \tilde{u}_{kn} + i\tilde{v}_{kn}$. The linearized map is then

$$\tilde{r}_{n+1} = \tilde{r}_n - C\sum_k \left[\varphi''_{k0}w_{k0}\tilde{r}_n + \varphi'_{k0}\tilde{u}_{kn}\right]$$
$$\tilde{\theta}_{n+1} = \tilde{\theta}_n + \frac{C}{r_0^2}\sum_k k\varphi_{k0}\left[kw_{k0}\tilde{\theta}_n + \tilde{v}_{kn}\right]$$
$$\tilde{u}_{k,n+1} = \mu_k\left[\tilde{u}_{kn} + \varphi'_{k0}\tilde{r}_n\right]$$
$$\tilde{v}_{k,n+1} = \mu_k\left[\tilde{v}_{kn} - k\varphi_{k0}\tilde{\theta}_n\right] \qquad (A3)$$

Perturbations $(\tilde{r},\tilde{u}_k)$ are decoupled from $(\tilde{\theta},\tilde{v}_k)$ and can be analyzed independently.

Radial perturbations $\tilde{r}_n = \tilde{r}_0 z^n$ and $\tilde{u}_{kn} = \tilde{u}_0 z^n$ must satisfy $\tilde{u}_{k0} = \mu_k\varphi'_{k0}/(z-\mu_k)\tilde{r}_0$ as well as

$$1 - z = C\sum_k \mu_k\left[\frac{\varphi_{k0}\varphi''_{k0}}{1-\mu_k} + \frac{\varphi'^2_{k0}}{z-\mu_k}\right] \qquad (A4)$$

When $C \ll 1$, all the solutions z should be in the neighborhood of $z = 1$. If $z = 1 - \epsilon$, then

$$\epsilon = \frac{C}{1 - C\sum_k \frac{\mu_k}{(1-\mu_k)^2}\varphi'^2_{k0}}\varrho''(r_0) \qquad (A5)$$

where

$$\varrho''(r_0) = \sum_k \frac{\mu_k}{1-\mu_k}\left[\varphi_{k0}\varphi''_{k0} + \varphi'^2_{k0}\right] \qquad (A6)$$

Therefore in the limit of small C and finite damping factors $\mu_k < 1$, radially-stable (resp. unstable) fixed points are found where $\varrho(r)$ is minimum (resp. maximum).

Azimuthal perturbations $\tilde{\theta}_n = \tilde{\theta}_0 z^n$ and $\tilde{v}_{kn} = \tilde{v}_{k0} z^n$ must satisfy $\tilde{v}_{k0} = -\frac{\mu_k k\varphi_{k0}}{z-\mu_k}\tilde{\theta}_0$ as well as

$$(z-1)\left[1 - \frac{C}{r_0^2}\sum_k \frac{k^2\varphi_{k0}^2\mu_k}{(1-\mu_k)(z-\mu_k)}\right] = 0 \qquad (A7)$$

Since $z = 1$ is always a solution, these azimuthal perturbations are never more than marginally stable. The other solution z increases from zero as damping factors μ_k are increased (i.e., as the forcing amplitude is increased). Therefore, for each fixed point r_0, there is a finite threshold in forcing amplitude for which the damping factors μ_k satisfy

$$\sum_k \frac{k^2\varphi_{k0}^2\mu_k}{(1-\mu_k)^2} = \frac{r_0^2}{C} \qquad (A8)$$

Above this threshold, there is at least one solution z larger than unity, so the corresponding fixed point becomes azimuthally unstable. This corresponds to the walking threshold.

This azimuthal destabilization gives rise to periodic solutions of the map (14) where the particle orbits at

constant speed around the center of the cavity: $r_n = r_1$, $\theta_n = \alpha n$ and $w_{k,n} = w_{k1}e^{-ik\alpha n}$ (the wave pattern also rotates). The walking velocity is then $r_1\alpha$. Plugging this solution in the iterated map yields

$$w_{k1} = \frac{\mu_k \varphi_{k1}}{e^{-ik\alpha} - \mu_k} \tag{A9}$$

$$r_1(1 - \cos\alpha) = C\sum_k \varphi_{k1}\varphi'_{k1}\mu_k \frac{\cos(k\alpha) - \mu_k}{1 - 2\mu_k\cos(k\alpha) + \mu_k^2}$$

$$r_1^2 \sin\alpha = C\sum_k k\varphi_{k1}^2\mu_k \frac{\sin(k\alpha)}{1 - 2\mu_k\cos(k\alpha) + \mu_k^2}$$

where $\varphi_{k1} = \varphi_k(r_1)$ and $\varphi'_{k1} = [d\varphi_k/dr]_{r_1}$. This system of equations for (r_1, α, w_{k1}) can be solved numerically.

Slightly above the azimuthal destabilization threshold, the orbital radius r_1 can be assumed to be as close to the fixed point radius r_0, so $r_1 = r_0 + \varepsilon$, with $\varepsilon \ll 1$. The angular velocity α then satisfies

$$\left[r_0 + C\sum_k \frac{\mu_k(1 + \mu_k)}{(1 - \mu_k)^3}k^2\varphi_{k0}\varphi'_{k0}\right]\frac{\alpha^2}{2} = C\varrho''(r_0)\varepsilon \tag{A10}$$

Since $\varepsilon \to 0$ when $\alpha \to 0$, orbital solutions do originate from the azimuthal destabilization of fixed points, here through a pitchfork bifurcation. Each orbit then directly inherits from the radial stability of its corresponding fixed point.

Orbit stability can be inferred from a perturbation analysis $r_n = r_1 + \tilde{r}_n$, $\theta_n = n\alpha + \tilde{\theta}_n$, $w_{k,n} = (w_{k1} + \tilde{w}_{k,n})e^{-ik\alpha n}$, where $\tilde{r}_n \ll 1$, $\tilde{\theta}_n \ll 1$, $\tilde{w}_{k,n} \ll 1$, and $w_{k1} = u_{k1} + iv_{k1}$. The linearized map is then

$$\tilde{r}_{n+1}\cos\alpha - r_1\sin\alpha(\tilde{\theta}_{n+1} - \tilde{\theta}_n) = \tilde{r}_n - C\sum_k \left[\varphi''_{k1}u_{k1}\tilde{r}_n - k\varphi'_{k1}v_{k1}\tilde{\theta}_n + \varphi'_{k1}\tilde{u}_{k,n}\right]$$

$$\tilde{r}_{n+1}\sin\alpha + r_1\cos\alpha(\tilde{\theta}_{n+1} - \tilde{\theta}_n) = \frac{C}{r_1}\sum_k k\left[\left(\varphi'_{k1}v_{k1} - \frac{\varphi_{k1}v_{k1}}{r_1}\right)\tilde{r}_n + k\varphi_{k1}u_{k1}\tilde{\theta}_n + \varphi_{k1}\tilde{v}_{k,n}\right]$$

$$\tilde{u}_{n+1,k} = \mu_k\left[\cos(k\alpha)\left(\tilde{u}_{k,n} + \varphi'_{k1}\tilde{r}_n\right) - \sin(k\alpha)\left(\tilde{v}_{k,n} - k\varphi_{k1}\tilde{\theta}_n\right)\right]$$

$$\tilde{v}_{n+1,k} = \mu_k\left[\cos(k\alpha)\left(\tilde{v}_{k,n} - k\varphi_{k1}\tilde{\theta}_n\right) + \sin(k\alpha)\left(\tilde{u}_{k,n} + \varphi'_{k1}\tilde{r}_n\right)\right].$$

Perturbations along different directions are now coupled, and eigenvalues can be found numerically.

2. Fixed points and orbits in the case of infinite memory

Fixed points do not exist anymore at infinite memory, at least as soon as more than one mode is selected. Indeed, they would require $\varphi_k(r_0) = 0$ simultaneously for all selected modes k. We can then look for circular orbits $r_n = r_1$, $\theta_n = \alpha n$, $w_{kn} = w_{k1}e^{-ik\alpha n}$. The wave equation imposes

$$w_{k1} = \frac{\varphi_{k1}}{e^{-ik\alpha} - 1}, \tag{A11}$$

which is finite provided that $k > 0$ (i.e., that no purely radial mode is selected). Then

$$u_{k1} = -\frac{\varphi_{k1}}{2}, \quad v_{k1} = \frac{\varphi_{k1}}{2}\frac{\sin(k\alpha)}{1 - \cos(k\alpha)}$$

$$r_1(1 - \cos\alpha) = -\frac{C}{2}\sum_k \varphi_{k1}\varphi'_{k1}$$

$$r_1^2\sin\alpha = \frac{C}{2}\sum_k k\varphi_{k1}^2 \frac{\sin(k\alpha)}{1 - \cos(k\alpha)}. \tag{A12}$$

In the limit of $(k\alpha)^2 \ll 1$,

$$u_{k1} = -\frac{\varphi_{k1}}{2}, \qquad v_{k1} = \frac{\varphi_{k1}}{k\alpha}$$

$$2\varrho_1 + \varrho'_1 r_1 = 0, \qquad r_1^2\alpha^2 = C\varrho_1, \tag{A13}$$

with

$$\varrho(r) = \sum_k \varphi_k(r)^2, \qquad \varrho(r_1) = \varrho_1, \qquad \left.\frac{d\varrho}{dr}\right]_{r=r_1} = \varrho'_1.$$

When the mode selection includes is at least one radial mode ($k = 0$), the orbit solution here above is not valid anymore, because v_{k1} blows up when $k = 0$. In the iterated map, the radial wave mode satisfies

$$w_{0,n+1} = w_{0,n} + \varphi_0(r_n) \tag{A14}$$

so the only way to avoid having this component to blow up is to impose $\varphi_0(r_1) = \varphi_{01} = 0$, which selects the orbital radii but leaves u_{01} and v_{01} undetermined. Moreover, if several radial modes coexist, there should not be any orbital solution.

The other wave components ($k > 0$) still satisfy

$$u_{k1} = -\frac{\varphi_{k1}}{2}, \qquad v_{k1} = \frac{\varphi_{k1}}{2}\frac{\sin(k\alpha)}{1 - \cos(k\alpha)} \tag{A15}$$

Then the particle equations become

$$r_1(1 - \cos\alpha) = C\left[\varphi'_{01}u_{01} + 2\sum_{k>0}\varphi'_{k1}u_{k1}\right]$$
$$r_1^2 \sin\alpha = 2C\sum_{k>0}k\varphi_{k1}v_{k1} \qquad (A16)$$

Again, these equations can be solved numerically to find the orbital radii r_1 and their corresponding α.

Appendix B: Wave energy

In a recent paper, Borghesi *et al.* [40] observed an equivalence between the kinetic energy of the walker and the energy stored in the wave field, although the former was one order of magnitude smaller than the latter. The dimensional ballistic speed of the walker is here given by $v_w \simeq 0.6\lambda_F f/N_c$, from which we infer the kinetic energy of the walker:

$$T = \frac{2\pi}{3}R_d^3 v_w^2 \simeq 0.75\chi\rho\frac{R_d^3\delta\Omega}{R_c^2}f^2 \qquad (B1)$$

where R_d is the droplet radius. The time-averaged energy of a mono-frequency wave field is given by

$$E_{wave} \simeq \pi\rho f^2\lambda\int_S \langle H_n^2\rangle dS = 2\pi^2\rho f^2\lambda\frac{\Omega^2}{R_c^2}\int_0^1\langle h_n^2\rangle r\,dr \qquad (B2)$$

where we check numerically for each subset $\mathcal{S}$ that

$$2\pi\int_0^1\langle h_n^2\rangle r\,dr = \sum_k\langle|w_k|^2\rangle \simeq \frac{\chi\Lambda_F^2}{8C}. \qquad (B3)$$

Therefore, the ratio between both energies is

$$\frac{T}{E_{wave}} \simeq \frac{6}{\pi}\frac{R_d^3\delta^2}{\lambda_F^3 R_c^2} \qquad (B4)$$

In this model, δ is not directly expressed as a function of other parameters, so it is unfortunately hard to conclude here if both energies are equivalent or not. The estimation of δ from more advanced bouncing and walking models [33] is left to future work.

[1] J. W. M. Bush, Annu. Rev. Fluid Mech. **47**, 269 (2015).
[2] J. W. M. Bush, Physics Today **68**, 47 (2015).
[3] M. Faraday, Philos. Trans. R. Soc. London **121**, 319 (1831).
[4] T. B. Benjamin and F. Ursell, Proc. R. Soc. London **225**, 505 (1954).
[5] K. Kumar and L. Tuckerman, J. Fluid Mech. **279**, 49 (1994).
[6] A. Eddi, E. Sultan, J. Moukhtar, E. Fort, M. Rossi, and Y. Couder, J. Fluid Mech. **674**, 433 (2011).
[7] O. W. Jayaratne and B. J. Mason, Proc. R. Soc. London A **280**, 545 (1964).
[8] T. Gilet and J. W. M. Bush, J. Fluid Mech. **625**, 167 (2009).
[9] T. Gilet and J. W. M. Bush, Phys. Fluids **24**, 122103 (2012).
[10] Y. Couder, E. Fort, C.-H. Gautier, and A. Boudaoud, Phys. Rev. Lett. **94**, 177801 (2005).
[11] T. Gilet, D. Terwagne, N. Vandewalle, and S. Dorbolo, Phys. Rev. Lett. **100**, 167802 (2008).
[12] T. Gilet and J. W. M. Bush, Phys. Rev. Lett. **102**, 014501 (2009).
[13] J. Molacek and J. W. M. Bush, J. Fluid Mech. **727**, 582 (2013).
[14] M. Hubert, D. Robert, H. Caps, S. Dorbolo, and N. Vandewalle, Phys. Rev. E **91**, 023017 (2015).
[15] Y. Couder, S. Protiere, E. Fort, and A. Boudaoud, Nature **437**, 208 (2005).
[16] A. Eddi, E. Fort, F. Moisy, and Y. Couder, Phys. Rev. Lett. **102**, 240401 (2009).
[17] Y. Couder and E. Fort, Phys. Rev. Lett. **97**, 154101 (2006).
[18] C. Richardson, P. Schlagheck, J. Martin, N. Vandewalle, and T. Bastin, arXiv (2014).
[19] A. Andersen, J. Madsen, C. Reichelt, S. Ahl, B. Lautrup, C. Ellegaard, M. Levinsen, and T. Bohr, Phys. Rev. E **92**, 013006 (2015).
[20] S. Perrard, M. Labousse, M. Miskin, E. Fort, and Y. Couder, Nat. Comm. **5**, 3219 (2014).
[21] E. Fort, A. Eddi, A. Boudaoud, J. Moukhtar, and Y. Couder, PNAS **107**, 17515 (2010).
[22] D. M. Harris and J. W. M. Bush, J. Fluid Mech. **739**, 444 (2014).
[23] A. U. Oza, D. M. Harris, R. R. Rosales, and J. W. M. Bush, J. Fluid Mech. **744**, 404 (2014).
[24] D. M. Harris, J. Moukhtar, E. Fort, Y. Couder, and J. W. M. Bush, Phys. Rev. E **88**, 011001 (R) (2013).
[25] D. Shirokoff, Chaos **23**, 013115 (2013).
[26] B. Filoux, M. Hubert, and N. Vandewalle, Phys. Rev. E **92**, 041004(R) (2015).
[27] S. Perrard, M. Labousse, E. Fort, and Y. Couder, Phys. Rev. Lett. **113**, 104101 (2014).
[28] M. Labousse, S. Perrard, Y. Couder, and E. Fort, New J. Phys. **16**, 113027 (2014).
[29] A. U. Oza, R. R. Rosales, and J. W. M. Bush, J. Fluid Mech. **737**, 552 (2013).
[30] T. Gilet, Phys. Rev. E **90**, 052917 (2014).
[31] P. A. Milewski, C. A. Galeano-Rios, A. Nachbin, and J. W. M. Bush, J. Fluid Mech. **778**, 361 (2015).
[32] J. W. M. Bush, A. U. Oza, and J. Molacek, J. Fluid Mech. **755**, R7 (2014).
[33] J. Molacek and J. W. M. Bush, J. Fluid Mech. **727**, 612 (2013).
[34] W. Batson, F. Zoueshtiagh, and R. Narayanan, J. Fluid Mech. **729**, 496 (2013).
[35] F. Blanchette, Phys. Fluids **28**, 032104 (2016).
[36] A. Eddi, D. Terwagne, E. Fort, and Y. Couder, Europhys. Lett. **82**, 44001 (2008).

[37] D. M. Harris and J. W. M. Bush, J. Sound and Vibration **334**, 255 (2015).

[38] L. de Broglie, Annales de la Fondation Louis de Broglie **12**, 1 (1987).

[39] L. de Broglie, "On the theory of quanta," Annales de Physique, 10e serie, t.III (1925).

[40] C. Borghesi, J. Moukhtar, M. Labousse, A. Eddi, E. Fort, and Y. Couder, Phys. Rev. E **90**, 063017 (2014).

[41] S. Kocsis, B. Braverman, S. Ravets, M. J. Stevens, R. P. Mirin, L. K. Shalm, and A. M. Steinberg, Science **332**, 1170 (2011).

[42] E. Nelson, Phys. Rev. **150**, 1079 (1966).